

Flight Performance of an advanced CZT Imaging Detector in a Balloon-borne Wide-Field Hard X-ray Telescope – *ProtoEXIST1* *

J. Hong, B. Allen, J. Grindlay

Harvard-Smithsonian Center for Astrophysics, Cambridge, MA 02138

S. Barthelemy, R. Baker

NASA Goddard Space Flight Center, Greenbelt, MD 20771

A. Garson, H. Krawczynski

Washington University in St. Louis and the McDonnell Center for the Space Sciences, St. Louis, MO 63130

J. Apple, W. H. Cleveland

NASA Marshall Space Flight Center and Universities Space Research Association, Huntsville, AL 35812

Abstract

We successfully carried out the first high-altitude balloon flight of a wide-field hard X-ray coded-aperture telescope *ProtoEXIST1*, which was launched from the Columbia Scientific Balloon Facility at Ft. Sumner, New Mexico on October 9, 2009. *ProtoEXIST1* is the first implementation of an advanced CdZnTe (CZT) imaging detector in our ongoing program to establish the technology required for next generation wide-field hard X-ray telescopes such as the High Energy Telescope (HET) in the Energetic X-ray Imaging Survey Telescope (*EXIST*). The CZT detector plane in *ProtoEXIST1* consists of an 8×8 array of closely tiled $2 \text{ cm} \times 2 \text{ cm} \times 0.5 \text{ cm}$ thick pixellated CZT crystals, each with 8×8 pixels, mounted on a set of readout electronics boards and covering a 256 cm^2 active area with 2.5 mm pixels. A tungsten mask, mounted at 90 cm above the detector provides shadowgrams of X-ray sources in the 30 – 600 keV band for imaging, allowing a fully coded field of view of $9^\circ \times 9^\circ$ (and $19^\circ \times 19^\circ$ for 50% coding fraction) with an angular resolution of $20'$. In order to reduce the background radiation, the detector is surrounded by semi-graded (Pb/Sn/Cu) passive shields on the four sides all the way to the mask. On the back side, a $26 \text{ cm} \times 26 \text{ cm} \times 2 \text{ cm}$ CsI(Na) active shield provides signals to tag charged particle induced events as well as $\gtrsim 100$ keV background photons from below. The flight duration was only about 7.5 hours due to strong winds (60 knots) at float altitude (38–39 km). Throughout the flight, the CZT detector performed excellently. The telescope observed Cyg X-1, a bright black hole binary system, for ~ 1 hour at the end of the flight. Despite a few problems with the pointing and aspect systems that caused the telescope to track about 6.4 deg off the target, the analysis of the Cyg X-1 data revealed an X-ray source at 7.2σ in the 30–100 keV energy band at the expected location from the optical images taken by the onboard daytime star camera. The success of this first flight is very encouraging for the future development of the advanced CZT imaging detectors (*ProtoEXIST2*, with 0.6 mm pixels), which will take advantage of the modularization architecture employed in *ProtoEXIST1*.

Key words: hard X-ray Imaging, CdZnTe, Coded-aperture imaging

1. Introduction

The high energy sky is active and dynamic, full of inherently variable sources as well as extremely luminous Gamma-ray Bursts (GRBs). Wide-field hard X-ray imaging is perhaps the only effective way to capture these unpredictable, energetic celestial events. The current GRB mission, *Swift*, to study GRBS, employs a large area (0.5 m^2) array of CdZnTe (CZT) detectors, each $4 \text{ mm} \times 4 \text{ mm} \times 2 \text{ mm}$ as separate pixels for coded-aperture imaging. The previously proposed *EXIST* telescope would have had 4.5 m^2 with 0.6 mm pixels [2]. A smaller (1024 cm^2) CZT imager incorporating the same 0.6mm pixels has now been proposed for the MIRAX experiment on the *Lattes* mission to be launched by Brazil [3]. The combination of a large area and fine pixels imposes serious challenges in detector design, packaging, and operations, given the limited power and space available in space missions.

We have been pushing the technology of advanced CZT imaging detectors required for future generation of wide-field hard X-ray imagers through our ongoing, three-part, balloon-borne wide-field hard X-ray telescope experiment, *ProtoEXIST*. We have successfully carried out a first high-altitude balloon flight of *ProtoEXIST1*, the first implementation of the program, which was launched from the NASA Columbia Scientific Balloon Facility (CSBF) at Ft. Sumner, New Mexico on October 9, 2009. *ProtoEXIST1* is a wide-field hard X-ray coded-aperture telescope, built to develop an efficient modularization and packaging architecture for a large area fine pixel CZT imaging detector (256 cm^2 with 2.5 mm pixels) and to demonstrate its performance in a near space environment. The X-ray telescope including the CZT detector performed very well during the flight. Here we report the detailed performance of the X-ray telescope and the imaging CZT detector during the flight. Full details of the detector and telescope system, including the assembly of the coded mask, the shields, the onboard calibration source and the interface to gondola will be presented in separate papers [4,5].

2. *ProtoEXIST1* Instrument

ProtoEXIST1 consists of a CZT detector plane, a

* Send correspondence to J. Hong :
E-mail: jaesub@head.cfa.harvard.edu

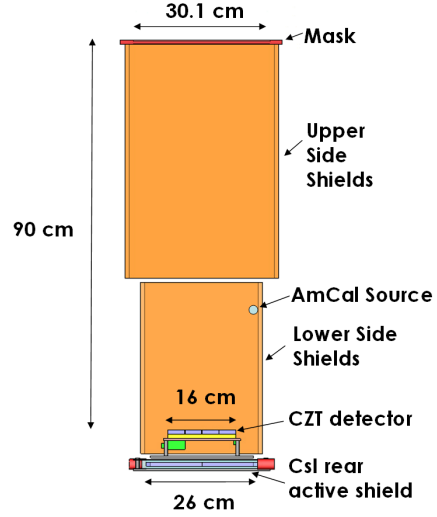


Fig. 1. Schematic view of *ProtoEXIST1*. The mask and the upper side shields are mounted on the top cover of the pressure vessel (PV), and the rest of the system is mounted inside the PV. See also Table 1.

Tungsten mask, passive side shields and a CsI rear active shield. The schematic view of the *ProtoEXIST1* telescope is shown in Fig 1. The key parameters of *ProtoEXIST1* are summarized in Table 1.

2.1. CZT detector plane

The CZT detector in *ProtoEXIST1* is a first implementation of a close-tiled fine pixel imaging CZT array in our program. Fig. 2 shows the detector assembly and the fully integrated detector plane in the flight configuration. An initial laboratory performance and the assembly procedure of the CZT detector plane for *ProtoEXIST1* are reported in [6] in detail. Here we review the modularization and packaging architecture and operational modes briefly.

The full detector plane covers $16 \times 16 \text{ cm}^2$ with 8×8 CZT crystals, providing 64×64 imaging pixels with 2.5 mm pitch. All of the 64 CZT crystals are tiled with a uniform gap ($\sim 900 \mu\text{m}$ for $19.5 \text{ mm} \times 19.5 \text{ mm}$ CZT), allowing the total active area of $15.6 \times 15.6 \text{ cm}^2$. This is a factor of $\gtrsim 8$ times larger in area than any previous tiled-pixelated CZT imagers of which we are aware.

The basic building block is a Detector Crystal Unit (DCU) that consists of a $1.95 \text{ cm} \times 1.95 \text{ cm} \times 0.5 \text{ cm}$ CZT crystal with 8×8 pixels bonded to an interposer board with a RadNET ASIC [7] underneath for readout (Fig. 2a). The traces on an interposer board connect the 2-D array of 8×8 anode

pixel pads on a CZT to a 1-D array of 64 channel input pads of the RadNET ASIC. In the next stage of assembly, a 2×4 array of DCUs are mounted on two vertically stacked electronics boards to make a Detector Crystal Array (DCA) (Fig. 2b). The DCA electronics boards contain four Analog-to-Digital Convertors (ADCs, AD7685BRM) and a Field Programmable Gate Array (FPGA, Altera Cyclone II EP2C20F256C7). The FPGA is programmed to have four independent data processing channels, each of which handles two DCUs with one shared ADC. We closely tile 2×4 DCAs on a motherboard, the FPGA-Controller Board (FCB), to complete the detector plane or Detector Module (DM; Fig. 2c). The FCB contains another larger FPGA (Altera Cyclone II EP2C20F484C7) to process 32 independent data streams (1 per 2 DCUs) from the FPGAs of the 8 DCAs. A network card (NetBurner¹, MOD5282) is mounted on the FCB to collect the science data from the FPGA and other HouseKeeping (HK) information, and pass them to a flight computer through an Ethernet port (see §2.3 and [5]). The FCB also reserves 8 TTL input lines for event tagging with ^{241}Am Calibration (AmCal, 200 nCi) and active shield trigger signals and for absolute timing using 1 pulse per second (PPS) pulses from the GPS unit on the gondola.

We obtain CZT crystals from Redlen Technologies², which produce high quality CZT at low cost through their patented traveling heater method. We bias 64 CZTs at -600V using two EMCO³ High Voltage Power Supplies (HV PS, C12N) mounted on the FCB. We apply the HV lead on the cathode using a thin ($50\text{ }\mu\text{m}$) Al tape, which is suitable for pressurized balloon flights and convenient for replacing DCU units if needed. The Redlen CZTs show $< 0.5\text{ nA/pixel}$ leakage currents under -600V . Each DCU is surrounded by Kapton-coated Copper RFI shields to minimize the observed interference between the units (see [6]). The shields kept the electronics noise down to the level of a single DCU operation.

CZTs were bonded on an interposer board (IPB) with two low-cost, low-temperature ($\lesssim 100\text{ }^\circ\text{C}$) techniques – initially with low temperature solder bonds from Delphon/QuikPak⁴ and then with Transient Liquid Phase Sintering (TLPS) bonds from Creative

Table 1
Telescope Parameters of *ProtoEXIST1*

Parameters	Values
Sensitivity (5σ)	$\sim 140\text{ mCrab/hr}^{\text{a}}$
Energy Range	$30 - 300\text{ keV}^{\text{b}}$
Energy Resolution	$3 - 5\text{ keV}$
Field of View	$19^\circ \times 19^\circ$ (50% Coding) $9^\circ \times 9^\circ$ (Fully Coded)
Angular Resolution	$20.3'$
CZT Detector	$64\text{ crystals} \times (2 \times 2 \times 0.5\text{ cm}^3)$
Area	$16 \times 16\text{ cm}^2$
Pixel, Thickness	$2.5\text{ mm}, 5\text{ mm}$
Tungsten Mask	$12\text{ layers} \times 0.3\text{ mm}$ thick
Coding Area	$30.1 \times 30.1\text{ cm}^2$
Pixel, Grid, Thickness	$4.7\text{ mm}, 0.5\text{ mm}, 3.6\text{ mm}$
Mask-Det. Separation	90 cm
CsI(Na) Rear Shield	$26 \times 26 \times 2\text{ cm}^3$
Side Passive Shield	Semi-graded Pb/Sn/Cu

^{241}Am Cal. Source $200\text{ nCi}, 36\text{ cm}$ above the detector

(a) assuming a 86% QE and a 45% dead time fraction with an observed ~ 250 cps background rate in the 30–200 keV band (see §4 and Fig. 8b), on-axis and no atmospheric absorption. (b) for imaging with $>80\%$ mask efficiency as limited by mask thickness; the detector energy range is $\sim 30 - 600\text{ keV}$.

Electron Inc⁵ for final DCUs. TLPS bonding was explored for possible future applications and one of its main advantages is that the resulting bonding is re-workable: the CZT can be detached and re-attached if needed.

The RadNet ASIC was chosen for *ProtoEXIST1* mainly because of its relatively low power consumption ($100 - 150\text{ }\mu\text{W/pixel}$) and the expected advance of the subsequent ASIC members in the same development family [7,8]. The low power consumption is an essential requirement for a large area CZT detector with fine pixels, which results in a large number of pixels or channels (e.g. 256k pixels in MIRAX). In addition, the RadNet ASIC provides a wide dynamic range with low electronics noise suitable for the hard X-ray band and allows flexible readout modes – multi-pixel pulse profile readout – for depth sensing (based on neighbor pixel charges, [9,10]) and event reconstruction of multi-pixel triggers arising from split charges or Compton scattering [6].

¹ <http://www.netburner.com/>

² <http://www.redlen.com>

³ <http://www.emcohightvoltage.com>

⁴ <http://quikpak.com>

⁵ <http://creativeelectron.com>

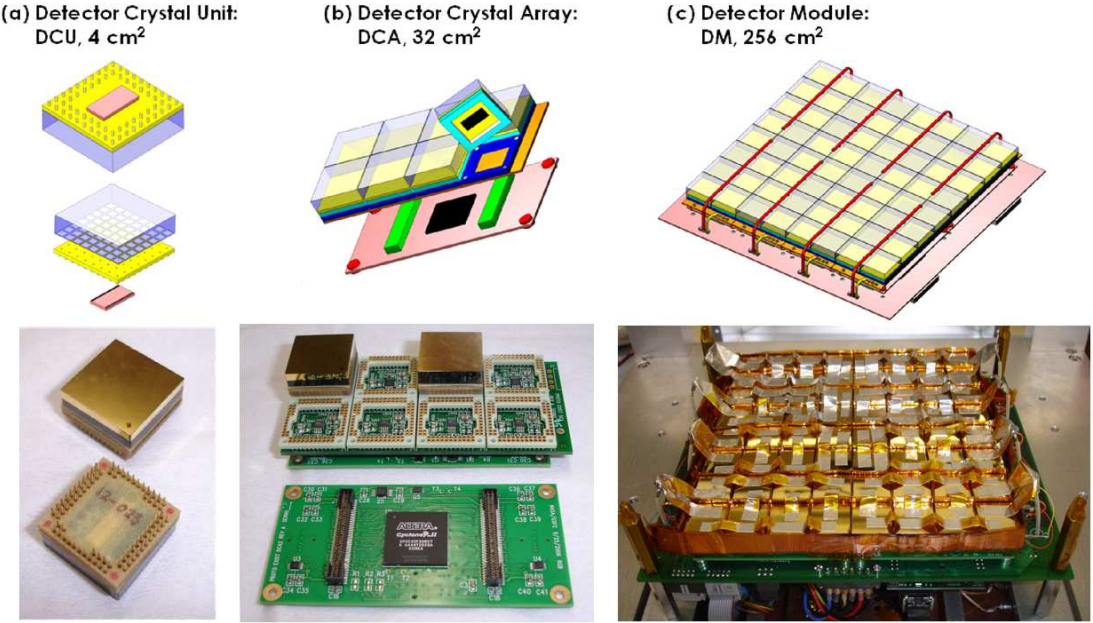


Fig. 2. The CZT detector assembly for the *ProtoEXIST1* imaging detector. (a) Detector Crystal Unit (DCU) consists of $2 \times 2 \text{ cm}^2 \times 0.5 \text{ cm}$ CZT bonded via an interposer board to the RadNET ASIC with 1-D 64 inputs (pink). (b) Detector Crystal Array (DCA) consists of a 2×4 array of DCUs. (c) Final view of flight Detector Module (DM) covers $16 \times 16 \text{ cm}^2$ with a 2×4 array of DCAs. HV bias (-600V) lines connect to the 4 DCAs on each side through Al tape "jumpers" between DCUs.

For *ProtoEXIST1*, we have implemented four readout modes for debugging, trigger, normal operation, or calibration (see Table 1 in [6]). During the flight, we operate the detector in the normal mode, where we read signals from eight neighbor pixels and two reference pixels in addition to the trigger pixels. The total number of neighbor pixels to read out varies, depending on the location of the trigger pixels: five for edge pixels and three for corner pixels. In *ProtoEXIST1*, we have not recorded the signals from adjacent crystals since the electrostatic shields prevent the charge induction across the crystals.

2.2. Mask, Shield and Onboard Calibration Source

The mask consists of 12 identical stacked layers of 0.3 mm thick Tungsten sheets, each of which has an identical pattern of a 2×2 uniformly redundant array (URA) chemically etched out in a 64 \times 64 square pixel configuration. In theory, URAs allow a perfect imaging response for a point source without coding noise. This particular URA pattern used for *ProtoEXIST1* is generated by perfect binary arrays [12], which allow a square mask pattern ideal for our detector geometry (see Fig. 4). The mask pixel pitch is a 4.7 mm with 0.5 mm grid to sup-

port isolated opaque elements. Therefore, the size of open elements is $4.2 \times 4.2 \text{ mm}^2$ and the total open fraction is 40% for normal incidence (the open hole fraction is 48%). The mask, mounted on a support frame, is located at 90 cm above the detector plane, and the URA pattern covers $30 \times 30 \text{ cm}^2$ (each mask sheet spans $36 \times 36 \text{ cm}^2$ for mounting), allowing a $10^\circ \times 10^\circ$ fully coded field of view (FoV) or $20^\circ \times 20^\circ$ for 50% coding fraction.

Graded passive shields made of Pb/Sn/Cu were used to limit the X-rays incident through the side of the telescope. These side shields are divided into two sections (Fig. 1). The upper section sits on top outside of the pressure vessel (PV), mounted all around the mask support tower above the top cover of the PV to the mask. The lower section is mounted onto a similar support tower inside the PV and covers all four sides of the detector plane above the rear active shield to the bottom side of the top cover of the PV. A part of the side shields was not completely covered with Sn/Cu, and so the lead sheets were partly directly exposed to the detector plane so that fluorescent X-ray K_α and K_β lines from the lead were observed in the spectrum (see §4.3). The thickness of the side shields are 2.6/0.7/0.4 mm (Pb/Sn/Cu) for the lower section, and 2.6/0.3/0.3 mm for the

Table 2
Science Data Size and Rate

Parameters	Values
Event header size ^a + checksum	48 Bytes
16 samplings per pixel	32 Bytes
Raw event size per N pixel readout	$48 + 32N$
Compressed event size per N pixel readout	$48 + 2N$
In normal readout mode,	
Average number of pixels for readout	9.12 pixels
Average size of raw event data	339.8 Bytes
Average size of compressed event data	66.2 Bytes
Measured total event count rate	~ 750 cps ^b
Raw data rate	2.2 Mbps
Compressed data rate	530 kbps

(a) This does not include the packet header added during the transfer between the FCB and the flight computer.
(b) At 39 km float altitude, and dominated by cosmic-ray induced events before shied rejection. X-ray background events (30–200 keV) are ~ 250 cps; see §4.2.

upper section.

In order to stop the albedo atmospheric X-rays and tag charged particle induced background events, an active shield of a 2 cm thick 26×26 cm² CsI(Na) scintillator crystal from Scintitech⁶ is mounted about 10 cm below the detector plane. The CsI scintillator is larger than the active area of the detector plane, extending out to the side shields in order to reduce the direct open path to the detector plane from outside. However, the current configuration leaves about 4 cm gap between the rear and side shields, allowing a high background rate during the flight (see §4.2). The optical scintillation photons are collected by two photomultiplier tubes (PMTs, Hamamatsu⁷ R1924A) on two opposite sides of the CsI crystal through edge-readout wave shifters. Preamps and subsequent electronics in a VME crate provide a pulse for tagging shield events. A PC-104 based computer (separate from the flight computer below) controls the VME electronics. The FPGA on the FCB monitors the two discriminator signals from the active shields, and if they occur within 2 μ sec of the X-ray triggers, the X-ray event is tagged.

In order to monitor the gain variations of the detector, a ²⁴¹Am calibration source (AmCal) was assembled and mounted. The AmCal source consists of

a 200 nCi ²⁴¹Am doped in a plastic scintillator (Isotope Products Laboratories⁸), which is coupled to a PMT (Hamamatsu R7400U). The scintillation light induced from the α particle coincident with a 60 keV X-ray is collected by the PMT and amplified through a separate channel in the shield VME electronics for tagging the Am events. In addition to the onboard calibration source, we can command all of the 64 RadNET ASICs to inject on-chip pulses into every pixel at a configurable frequency, and we read them out in the same way as normal X-ray events. This monitors the dead time and the electronics gain variation of the readout system throughout the flight.

The fully assembled detector plane (Fig. 1c) is mounted on an Al frame and surrounded by a thin copper box on the four sides and the rear side, which forms a detector shield enclosure. The top cover of the enclosure box is a 150 μ m thick Al sheet. Two fans are mounted on the side of the enclosure and another two on the bottom for temperature control through air (N₂) circulation through the PV. The fan power is electrically isolated from the power for the detector plane to minimize the electronics noise.

2.3. Flight Computer, Data Rate and Transfer

The flight computer is a 2 GHz Intel dual core compact PC (AEC-6920 by AAEON Technology⁹) with a 128 GB solid state disk designed to operate in extreme environments. The flight computer collects the science and HK data from the FCB through Ethernet links, stores them on the onboard hard disk, and sends a compressed version of the data to the transmitter (see below). It also issues to the FCB the commands uploaded through a RS422 port from the gondola computer [5]. In order to handle these tasks, the flight computer runs three basic programs – a command listener (CL) program, a data acquisition (DAQ) program, and a transmitter handler (TH) program under a linux (Fedora 8) operating system. A cron job based watchdog script monitors the health of these three programs, and terminates or relaunches them automatically if needed.

Table 2 summarizes the data size and measured rate (see also Fig. 6). The raw data rate is about 2200 kbps for 750 cps. The DAQ program saves the entire raw data stream on the onboard solid state hard disk. In order to meet the telemetry limit (400 kbps),

⁶ <http://www.scintitech.com>

⁷ <http://www.hamamatsu.com>

⁸ <http://www.isotopeproducts.com/>

⁹ <http://www.aaeon.com>

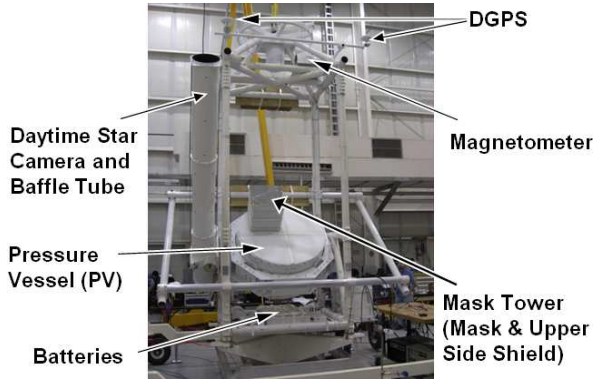


Fig. 3. The overview of the payload and gondola.

the DAQ program also compresses the data by calculating a single pulse height value from 16 samples of the pulse profile (see Fig. 2 in [6]), and sends only the resulting pulse height instead of the full 16 samples to the TH program. The corresponding compressed data rate is about 530 kbps, which is about 24% of the raw data rate instead of 8% (1/16th) due to the overhead of the event header. The compressed data rate can still exceed the telemetry rate. Therefore, the DAQ program monitors the data rate, and drops a fraction of events randomly (only for telemetry) to meet the telemetry bandwidth so that the full data stream for a given event can be transmitted to the ground during the flight. The data reduction fraction for telemetry is continuously adjusted during the flight to keep the compressed data rate below 300 kbps, which allows a 100 kbps margin for the packet header, the HK data or possible variations of the telemetry limit. For debugging purpose, the DAQ program can also send the raw data without compression at request. Transmission modes (raw or compressed) and the data reduction fraction for the telemetry can be controlled by the commands uploaded from the ground.

In addition to the science data, the HK data and the command echo are merged and transmitted to the ground without any compression since their rate is relatively small. There are four major HK data streams: the FCB HK data reporting the various input voltages and currents including the HV PS and the temperature of the FCB, the shield HK data reporting the active shield and AmCal count rate and status of the HV PS for PMTs, the DAQ HK data reporting the status of the flight computer such as free hard disk space, and the Power HK data reporting the power input voltages and the currents coming into the PV and temperatures and pressures

of a few points inside the PV. On the ground, we monitor and save the transmitted data, and issue commands accordingly.

3. Payload Integration and Test

The detailed description of the payload integration is found in [4,5]. Here we briefly summarize the integration and test of the detector plane.

The CZT detector plane for the *ProtoEXIST1* telescope was fully assembled (Fig. 1c) at Harvard University on 2009 August 31. In September, 2009, the detector plane was mounted inside the PV along with the side passive shields, the CsI rear active shield, the AmCal source and the electronics. Then, the *ProtoEXIST1* telescope payload - the PV and the mask tower - was integrated into the Harvard gondola now including a new pointing and aspect control system consisting of a daytime star camera, differential global positioning system (DGPS) units, and a magnetometer (Fig. 3) [4,5].

After the payload integration, we irradiated the X-ray telescope using a ~ 5 mCi ^{57}Co radioactive source. The source was positioned about 6.5 m away from the mask within a few degrees of the X-ray telescope axis. Fig. 4a shows the detector count map of the source in the 80 – 150 keV band from about 15 min of the irradiation of the ^{57}Co source. For illustration, the 2×2 URA mask pattern is shown in Fig. 4b with a section highlighting the matched pattern observed in the detector image. Fig. 4c shows the reconstructed sky image of the fully coded FoV using a balanced cross-correlation (e.g. see [11]) between the mask pattern and the detector image and accounting for magnification of the shadow pattern due to the finite source distance. The measured S/N (~ 80) of the source is a bit lower than the Poisson-noise based S/N because of the coding noise introduced by incomplete sampling (91%) of a full cycle of the URA pattern due to magnification.

For energy calibration, we use the pre-flight radiation data using the ^{57}Co source. For a given pixel at a given trigger capacitor, we identify the raw ADC values of three known energies - zero keV from the reference pixel measurements, 122 keV from the ^{57}Co source and 650 keV from the internal pulser inputs - by a fit using a gaussian function to the raw spectra. The conversion from other raw ADC values to energies uses a 2nd order polynomial fit between the raw ADC values and X-ray energies of the three known values [9]. After this relatively quick calibra-

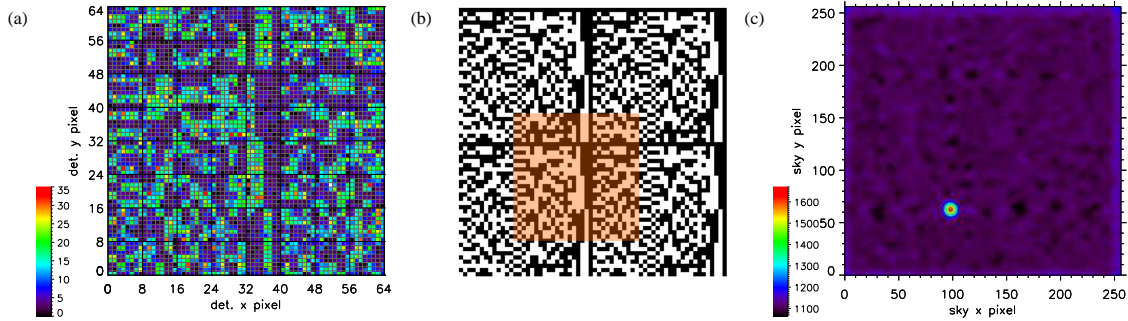


Fig. 4. (a) The detector count map generated by a 15 min irradiation of an external ^{57}Co source at 6.5 m away from the telescope. (b) The 2×2 URA mask pattern: the (orange) shaded section of the mask pattern indicates the coding area of this particular configuration. (c) The reconstructed sky image in the fully coded FoV using 5.35 mm magnified mask pixel pitch.

tion, the detector shows about 4 keV FWHM at 60 KeV lines and 10 keV at 120 keV. The latter indicates that there is room for improvement in the calibration (see [9,6,5]): e.g. the pulser is a less reliable energy calibrator, and the charge split or depth correction is not performed.

The tagging efficiency of the AmCal events in the CZT detector is measured about 74% (see §4.2), and does not increase with the coincidence window as long as the window is longer than 2 μsec . Therefore, the other 26% AmCal events are suspected to fail to generate a tagging signal all together probably due to insufficient light collection in the PMT from the 5 MeV α particle of ^{241}Am decays near the edge of the scintillator. The tagging efficiency of high energy charged particles by the CsI shield is estimated to be around 50% on the ground, based on the high energy events induced by atmospheric muons, which are recorded near the upper limit (~ 1 MeV) of energy deposit for a pixel. This is roughly consistent with the solid angle coverage of the rear shield. This tagging efficiency is likely energy dependent.

4. Flight Performance

4.1. Flight Overview

After 6 previous launch attempts, early in the morning on Oct 9, 2009, all the systems were checked twice with an external power supply for flight, and then before balloon inflation began, they were switched to the onboard battery, waiting for launch. The procedures for the initialization sequence of the detector are, in order: powering up the system, activating the internal ASIC pulsers, disabling the known hot pixels, applying the HV bias on the CZT crystals at -600 V (gradually ramped

up over ~ 10 min), and setting the DCU thresholds gradually down to ~ 30 keV over ~ 15 min. Each DCU has its own unique threshold setting but all 64 pixels in a DCU share a common threshold. The complete sequence takes about 30 min and each procedure can be either manually or autonomously executed. The internal ASIC pulsers were run in all of the 64 DCUs at 0.3 Hz throughout the flight for a dead time calibration. The active shield system is also initialized right after power-up.

The payload was launched at 14:30 UT by a 40 million m^3 high altitude balloon from the NASA CSBF at Ft. Sumner, New Mexico. Fig. 5 shows (a) the inflated balloon bubble (top $\sim 1/4$ of the balloon) right before the launch, (b) during the liftoff and (c) the flight path on a Google map. Fig. 6 shows the aspect and pointing history of the system during the flight and the raw count rate history of several key event types recorded in the detector system. The payload reached the float altitude of 40 km at 17:00 UT (blue in Fig. 6a). The flight duration was only about 7.5 hr with 5.5 hr at float altitude due to strong winds (~ 60 knots) and it was terminated near Hayes, Kansas, due to both the ~ 500 km telemetry limit and the NASA safety regulations that prohibit flights over densely populated area. The landing was relatively harsh due to high surface winds, and the gondola frame sustained some damage, but the payload was recovered without any damage.

When the payload reached the float altitude, the Crab pulsar, one of a few sources bright enough for detection in a short observation for a hard X-ray telescope of this moderate size, had just set. Until Cyg X-1 rose about 4 hr later, we successfully performed a number of system checks such as shield threshold tests (18:00 UT), while attempting tracking 3C 273. From 21:00 UT, we observed Cyg X-

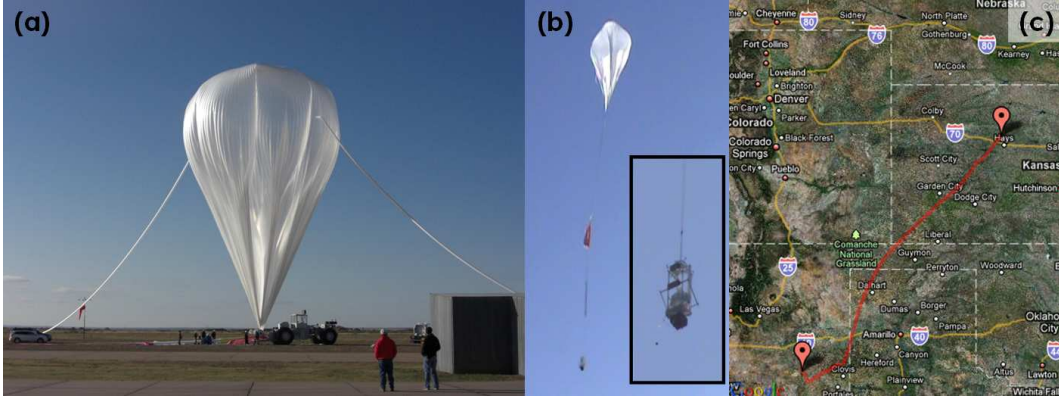


Fig. 5. The inflated balloon "bubble" (top $\sim 1/4$ of balloon) right before the launch (a), the liftoff (b) and the flight path on a Google map (from Ft. Sumner, New Mexico to Hayes, Kansas) (c). The inset in (b) shows the payload during the liftoff.

1 until the termination of the flight. After an hour observation of Cyg X-1, we reset the power of the detector system at 22:00 UT for a test. The system came back up without a glitch. After the power reset and the initialization sequence, we had less than a 10 min of fine-pointed observation of Cyg X-1 before we were requested to terminate the flight.

The X-ray telescope performed excellently throughout the flight, but the aspect and pointing system suffered a few major issues: until in the middle of the Cyg X-1 observation, the telescope could not track a target properly. First, we lost the DGPS units, possibly due to insufficient thermal insulation, at around 15:46 UT during the ascent. Second, a malfunction of the star camera software disabled the live feedback to the pointing system and forced us to rely on the magnetometer and the elevation axis for target tracking. The absolute error of the raw azimuth values reported by the magnetometer can be as large as 10° without calibration, depending on the orientation. Third, the elevation axis failed to follow the target properly until stabilized later in the flight (21:55 UT), likely due to insufficient torque for the motors.

Despite these issues, Cyg X-1 was within the partially coded FoV above 60% coding fraction and it was mostly $\lesssim 2\text{--}3^\circ$ off in the elevation axis and $6\text{--}7^\circ$ off in azimuth from the X-ray axis (see Fig. 12). We calibrated the raw azimuth values using those reported by the DGPS units during the ascent before they failed when the payload was freely spinning (14:30 - 15:46 UT; black line in Fig 6a). This calibration reduces the absolute error of the azimuth down to $\sim 1\text{--}2^\circ$. Fortunately, a set of the sky images captured by the star camera were later identified and used to verify and correct the aspect and

pointing history derived by the magnetometer and the elevation axis. The time stamps of these images are marked by (green) 'X's at the right-most side in the top panel of Fig. 6.

4.2. Event Rate

Fig. 6b shows the raw count rate history of the detector system during the flight. The total event rate (black) is the total trigger rate in the detector system, which is dominated by the cosmic ray induced interactions. The shield tagged event rate is shown in red, and the X-ray event rate (blue) is from the events without a shield tag. The AmCal rate (purple) is the event rate with an AmCal tag. The pulser rate (green) is the internal ASIC pulser rate. Note that each raw event is recorded in a unit of a DCU pair, counting a multi-pixel trigger event as one event but counting a multi-DCU-pair trigger event as multiple events. The latter means that the 0.3 Hz pulser injected over the entire detector plane should be recorded with rate $0.0394 \text{ counts s}^{-1} \text{ cm}^{-2}$ when there is no dead time¹⁰.

The absolute timing accuracy of events is in an order of $0.5 \mu\text{s}$, which is determined by the sampling frequency of the RadNET ASIC. We save the time tag of each event with a 0.1 ms resolution. A typical readout time for an event with a 10 pixel readout is about 5 ms, which leads to a dead time for event readout in a given DCU pair, but not for the rest of the DCU pairs since each DCU pair operates independently. The analysis show that almost all of the X-ray events with multi-pixel triggers in a DCU pair

¹⁰ $0.0394 = 0.3 \text{ Hz} \times 32 \text{ DCU pairs} / 243.4 \text{ cm}^2$, where the detector area is $1.95 \times 1.95 \text{ cm}^2 \times 64 \text{ DCUs}$.

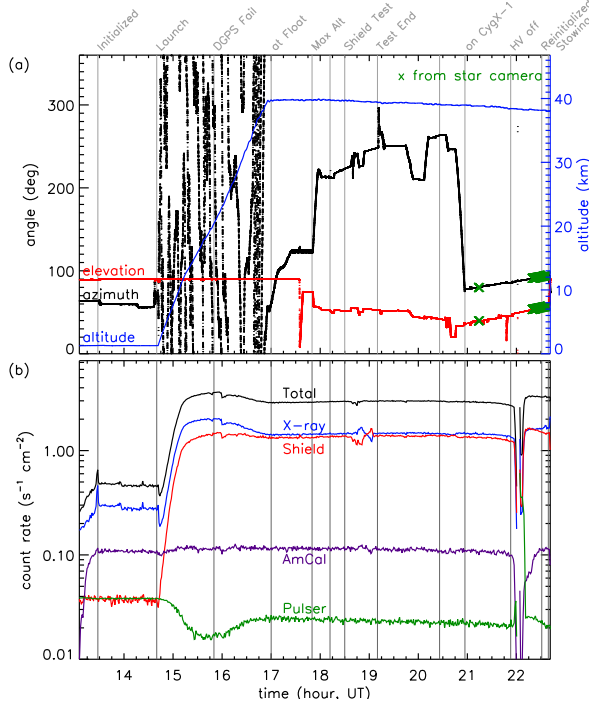


Fig. 6. (a) The aspect and pointing history of the flight. The azimuth angles (black) are based on the DGPS-calibrated magnetometer, and the elevation angles (red) are based on the elevation axis. The altitude (blue) is recorded by external pressure gauges. The (green) 'X's mark the azimuth and elevation values driven by a set of sky images captured by the star camera. The top axis labels the key events of the flight. (b) The raw detector count rate history of the flight. From top, the total event rate (solid black), the X-ray event rate (blue), the shield tagged event rate (red), the AmCal tagged event rate (solid blue), and the pulser event rate (green). The dip in pulser rate at 15–16 hr is due to increased dead time at the high count rates encountered in the Pfoetzer maximum in balloon ascent.

are truly simultaneous (not a random coincidence of multiple events), whereas about 9% or less of the X-ray events with multi-DCU triggers are truly simultaneous. In the case of multi-pixel triggers, almost all of the X-ray events are four pixel triggers or less. Therefore, for imaging and spectral analysis of Cyg X-1 and the AmCal events, we mainly focus on the low energy X-ray events with four pixel triggers or less, and we consider all the low energy X-ray events with multi-DCU-pair triggers as independent events. For the charged particle induced events with a shield tag, about 30% triggered multiple DCU pairs. Many of them are truly simultaneous, generating large tracks (Fig. 7), which illustrates a potential of large area CZT imaging detectors as cosmic ray detectors.

The raw X-ray event rate in Fig. 6b contain Am-

Cal events due to missing tags and is not corrected for dead time. To extract the proper X-ray event rate and spectra, we use the following relations.

$$r_X = f_{\text{Live}}(R_{\text{Am}} + R_X) - r_{\text{Am}} \quad (1)$$

$$r_{\text{Am}} = f_{\text{Live}}(f_{\text{AT}}R_{\text{Am}} + f_{\text{RT}}R_X) \quad (2)$$

where f_{Live} , f_{RT} , f_{AT} are the live time fraction, the random coincidence fraction by AmCal tag and the AmCal tagging efficiency respectively, and r_X and r_{Am} are, respectively, the measured raw count rates of the X-ray events (no shield or AmCal tag) and the AmCal events (an AmCal tag, but no shield tag); R_X and R_{Am} are the corresponding true count rates (i.e. the incident rate if the detection efficiency is 100%). Fig. 8 shows these corrected rates (R_X and R_{Am}) for various cases and Fig. 9 for the energy spectra before and after correction.

The live time fraction (f_{Live}) is estimated based on the captured internal pulser fraction and random coincidence rate of AmCal tagging (f_{RT}) is estimated based on hard X-ray events in the 80–200 keV band where all the AmCal tagged events are due to random coincidences. (Fig. 8a). Pulser events are easy to identify due to simultaneous injection of 650 keV equivalent signals into all 128 pixels of each DCU pair, which produce a narrow line around 83 MeV (for summed pixels) in the pulse height histogram. (e.g. green in Fig. 9c). The pulser recovery fraction ($= f_{\text{Live}}$) is about 97% on the ground, and it dropped down to 40% during the ascent due to a large increase of background, and then stayed around 55–60% during the flight.¹¹ Fig. 8a (red) shows f_{RT} stayed fairly constant throughout the flight. For the rest of the calculation, we use the average value of f_{RT} , 3.6%.

We set f_{AT} so that the resulting energy histogram of the X-ray events free of the AmCal events shows no positive or negative bump around the 60 keV (black curve in Fig. 9b). We did this for both the flight spectra and the prelaunch ground spectra, and for f_{Live} , we use the average value of each data set. In order to have a smooth continuum at 60 keV, the

¹¹The event readout time in a DCU pair ranges from ~ 5 to 25 ms, depending on the number of readout pixels. For an event occurrence rate of 1500 cps over the full detector plane, which is equivalent to about 47 cps per a DCU pair, the event capture fraction under an on-average ~ 15 ms event readout time would be about 50% ($= \exp(-47 \times 1.5 \times 10^{-2})$). Therefore, the observed total event rate of ~ 750 cps is consistent with the $\sim 50\%$ live time fraction.

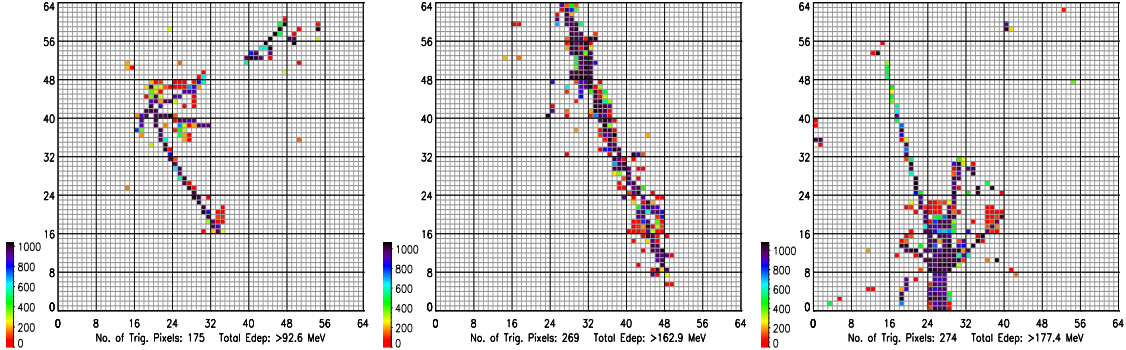


Fig. 7. Examples of multiple DCU trigger events induced by cosmic ray interactions during the flight. The number of the simultaneously triggered pixels and the total energy deposited by the events are labeled. The color scale shows the energy deposit in each pixel in keV. Since the energy deposit is saturated at ~ 1 MeV, the recorded total energy deposit is a lower limit.

allowed range for f_{AT} is between 0.735 and 0.740; we therefore used 0.738 for f_{AT} for the calculation.

Fig. 8b shows the corrected total event (gray), X-ray event (black) and AmCal (red) event rates. The total event rate (grey) reached about 9 counts $\text{s}^{-1} \text{cm}^{-2}$ during the ascent and dropped to 4.5 counts $\text{s}^{-1} \text{cm}^{-2}$ at the float altitude and gradually increased to 5.4 counts $\text{s}^{-1} \text{cm}^{-2}$ later in the flight. The X-ray event rate (black) stayed about 2.3 – 2.7 counts $\text{s}^{-1} \text{cm}^{-2}$ at the float altitude. Since the trigger rate in the CsI shield (~ 100 keV threshold), which likely represents the charged particle induced event rate, (not shown in the figure) was 2.1 – 2.7 counts $\text{s}^{-1} \text{cm}^{-2}$, the combined rate of the X-ray and charged particle induced events makes up the observed total count rate of 5.4 counts $\text{s}^{-1} \text{cm}^{-2}$. However, the X-ray event rate still contains a large fraction of charged particle induced events, considering the relatively low shield tagging efficiency ($\sim 50\%$, §3), a higher threshold of the CsI shield, and secondary background due to interactions in the surrounding side shield and mounting structures. To resolve the precise composition of the X-ray background rate, detailed Monte-Carlo simulations of X-ray and charged particle transport in the telescope geometry are needed.

The low energy X-ray events (30–200 keV, blue) stayed at around 0.86 – 1.1 counts $\text{s}^{-1} \text{cm}^{-2}$. If we assume a shield tagging efficiency of 50% (§3), the low energy X-ray event rate was about 0.5 – 0.7 counts $\text{s}^{-1} \text{cm}^{-2}$ (purple). Assuming an albedo X-ray flux of $13.9E^{-1.81} \text{ ph cm}^{-2} \text{ s}^{-1} \text{ keV}^{-1}$ at 3.5 g cm^{-2} [13] and an aperture FoV of 0.1 sr (FWHM) with a 40% open fraction, we expect the aperture X-ray background rate of ~ 0.04 counts $\text{s}^{-1} \text{cm}^{-2}$ in the same band. In addition, the gap between the rear and side

shields allows a projection-corrected FoV of 0.5 sr, which can contribute ~ 0.45 counts $\text{s}^{-1} \text{cm}^{-2}$. We also estimate a total flux of ~ 0.1 counts $\text{s}^{-1} \text{cm}^{-2}$ in the Pb fluorescent X-rays. The combined aperture and leakage X-ray flux in the 30–200 keV band is estimated to be ~ 0.6 counts $\text{s}^{-1} \text{cm}^{-2}$, which is consistent with the observed X-ray event rate. This estimate lacks some details such as attenuation by surrounding structures for X-rays coming below, the contribution from the internal background or an increase of the active area due to gaps between CZTs but their effects are rather small or their contributions cancel each other to some extent.

The corrected AmCal rate (R_{Am} , red) stayed relatively constant at 0.128 ± 0.006 counts $\text{s}^{-1} \text{cm}^{-2}$, indicating our analysis works well. Based on the known source strength of the AmCal sources with $\sim 2\%$ attenuation from the detector enclosure window, etc, one can calculate the overall detection efficiency at 60 keV to be 0.86 ± 0.04 ; the $\sim 10\%$ loss of QE is due to a variety of effects (dead surface layer, etc) and will be reported for several energies in [5]. The photo-peak efficiency in the 55 – 65 keV range is 0.54 ± 0.02 . The error values are only of statistical origin, and the simplified geometric assumption of a point source can add an additional 5% systematic error.

4.3. Detector Spectra

Fig. 9 shows the energy histograms of various event types before and after correction by Eq. 1 and 2 in §4.2. The top panels show the low energy section of the histogram in photon flux, and the bottom panels show the full range of the histogram in energy flux unit. Fig. 9d breaks up the X-ray events (no shield tag, no AmCal tag) by the number of

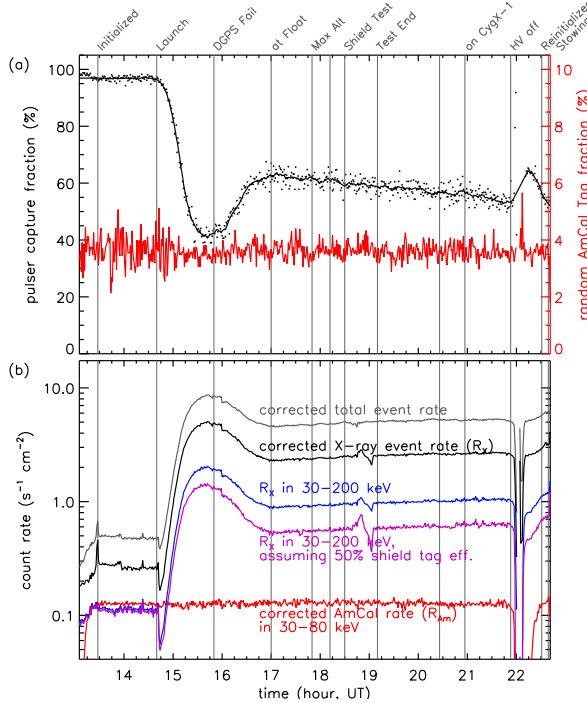


Fig. 8. (a) The pulser capture fraction (= the live time fraction, black) and random tagging fraction of the AmCal source events (red). (b) The count rate history of the corrected data by Eq. (1) & (2). Note the correction fixes only the untagged AmCal event rate, so that the X-ray event rate still includes contributions from the charged particle induced events.

triggering pixels. The flight data in the figure are from the events recorded between 17:50 and 21:53 UT, and the ground data between 13:35 and 14:40 UT. In the case of the corrected AmCal spectra the ground data (not shown) agree with the flight data (red in Fig. 9b & c). Note that, after correction, the AmCal spectra lack high energy events (>65 keV).

A 5 mm thick CZT detector is about 80% transparent to 500–600 keV photons, and the higher energy events in the spectra are mostly from the multi-pixel triggering events such as the charged particle induced events and the pulser events at 83 MeV (green) (Fig. 9c). The peaks at 75 and 85 keV are due to the K α and K β lines of the lead fluorescent X-rays as aforementioned. A mild bump around 511 keV originating from electron positron pair production is visible in the single pixel trigger event (blue) of Fig. 9d. The origin of the peak at ~ 1 MeV is not cosmic but is due to the upper limit of the dynamic range of the ASIC preamp channel (i.e. the maximally allowed energy deposit for a pixel), and the multi-pixel readout generates the additional peaks at its multiples around 2 and 3 MeV.

4.4. Temperature Dependent Gain Variation

The detector system is mounted inside of the PV, which is pressurized with dry N₂ and thermally controlled by a set of heaters and fans. The detector module experienced a $\sim 10^\circ\text{C}$ temperature variation during the flight. Fig. 11 shows the AmCal spectra summed over the entire detector plane as a function of time in comparison with the temperature variation (blue). For easy comparison, the energy histogram is renormalized at each time bin. The figure shows that the detector gain correlates with the temperature (ΔE (keV) $\approx 0.116\Delta T$ ($^\circ\text{C}$)). The temperature dependent gain change is likely due to the capacitance variation of sampling capacitors in the ASIC, and the CZT properties do not change observably over this temperature variation. A similar trend is observable with the pulser run. Unlike the gain, the energy resolution does not vary much with the temperature. For more information on the temperature dependent detector response of the *ProtoEXIST1* detector, see [5].

5. Imaging Cyg X-1

We observed Cyg X-1 for about 100 mins at the end of the flight. After an hour into the observation, which had large pointing excursions (mostly in elevation; see Fig. 12a), we performed a power cycle test of the detector system, which took about 30 min. Thus we have a total of an hour and ten minutes of usable data with only the final 10 min having relatively stable ($\pm 10'$) pointing (see Fig. 12). Here we describe the aspect calibration, image processing and detection of Cyg X-1 as well as its measured energy spectrum.

5.1. Image Reconstruction

The event distributions in the detector observed during the flight are substantially different from those measured on the ground. For instance, the dominance of charged particle interactions increases the fraction of multi-pixel events, which more likely produce an artificial pattern of event distribution. In low energy X-ray events with ≤ 4 pixel triggers, there are a few factors causing the non-uniformity in the event distribution in addition to the usual pixel or crystal dependent efficiency variation. Fig. 10a shows an example raw detector image of single pixel trigger events. In order to visualize the

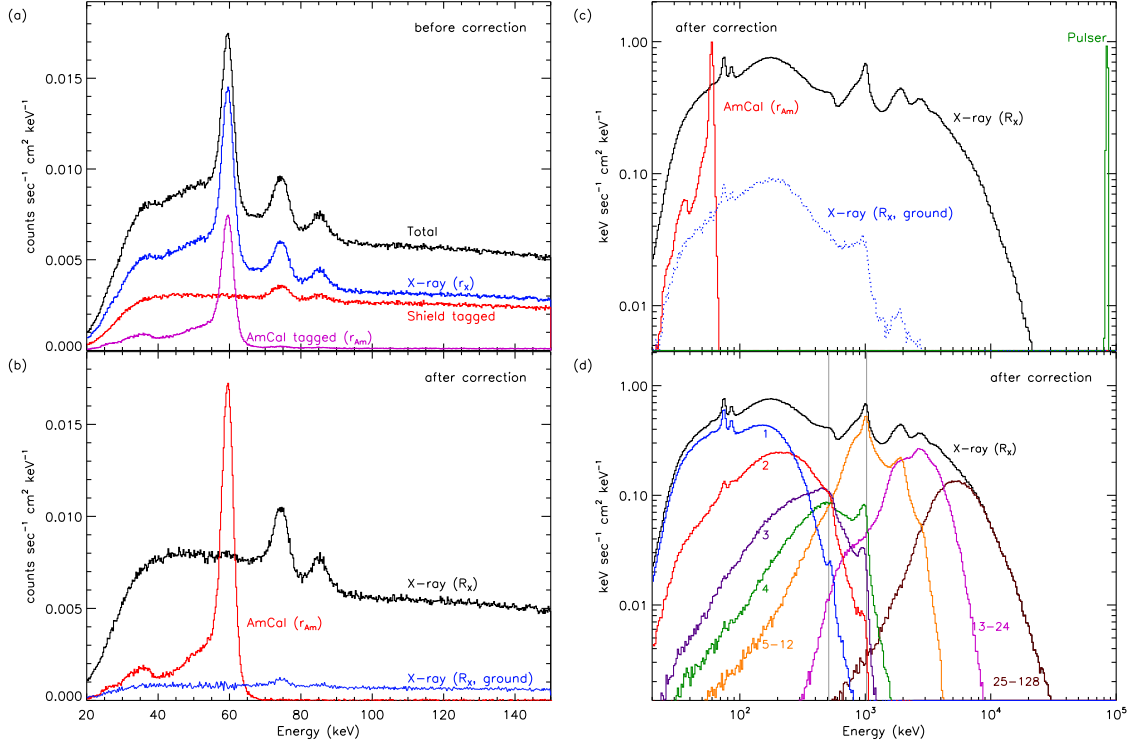


Fig. 9. (a) The energy-calibrated observed flight spectra classified by shield and AmCal tags, (b) & (c) the corrected flight spectra by Eq. 1 & 2 in comparison with the corrected ground X-ray spectra (blue), and (d) the corrected flight spectrum of the X-ray events and their composition by the (labeled) number of triggering pixels. The left panels show the spectra in the photon flux and the right in the energy flux with a wider energy range. In (a), the X-ray spectra (r_X) represent events without an AmCal or shield tag, but they still contain the AmCal events, as indicated in a large peak at 60 keV. After correction in (b) and (c), the X-ray spectra (R_X) do not have any contribution from the AmCal source. In (c) the X-ray spectra of the corrected flight data (black) are substantially brighter than those of the ground data (blue), but the AmCal and pulser spectra of the corrected flight data are nearly identical to those of the ground data (not shown). The vertical lines in (d) mark 511 keV and the maximally allowed energy deposit in a pixel (~ 1 MeV); higher energy peaks are due to 2 or 3 pixel pileup.

non-uniformity more clearly, we also show the event distribution folded onto a DCU pair (i.e. all 32 DCU pairs are stacked), as illustrated in the small panel. In this example, the first noticeable non-uniformity is the count enhancement of the edge pixels due to gaps (900 μ m for 1.95 cm \times 1.95 cm crystals) between CZT crystals that provide additional surface area for accepting off-axis X-ray events. In addition, the current sequential readout scheme performed in an increasing order of pixel number makes the data of the last few pixels more susceptible to corruption. In summary, non-uniformities in the detector image have various origins: for some, the cause is obvious and for others, not. For imaging, we rely on background subtraction to eliminate the non-uniformities regardless of their cause. We also explored an option of using a synthetic background pattern for subtraction, which was generated based on the observed non-uniformities. The synthetic

background pattern does not work as well, which is likely due to unknown and thus missing components of the non-uniformities in the synthetic pattern.

We generated a background detector plane image using the data set between 18:30 and 20:58 UT, which is just before pointing on Cyg X-1 and so the closest in-flight background free of bright X-ray sources. Then we subtracted the scaled (for total counts) background image from the detector plane images of the observation. Note the overall background rate varies with altitude and elevation, but the pattern of non-uniformities appears less sensitive to altitude or elevation as demonstrated by the uniformity of the background subtracted images below (Fig. 10b). Since the background dominates the source counts (< 5%), the scale factor used for background subtraction is simply the ratio of the total count of the observation to the total count of the background image, which makes the total counts of

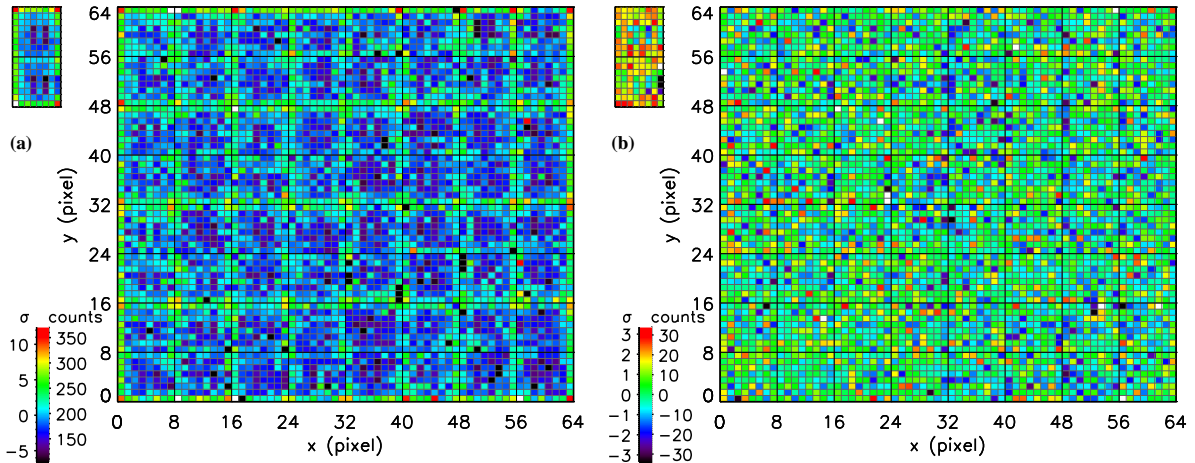


Fig. 10. Example detector plane images for single pixel trigger events in 30 – 200 keV: (a) before background subtraction, the count varies from pixel to pixel more than 10σ above the average and (b) after background subtraction, the variation is within $\sim 3\sigma$. The DCU-pair folded event distribution in the left top of each panel reveals the non-uniformity more clearly before the background subtraction: e.g. an excess of edge pixel counts and a deficit in a pattern that resembles the number '11'.

the subtracted image zero. The detector had 37 dead or disabled pixels (out of 4096 total), which include two pixels disabled during the flight. Even after disabling these hot pixels, there are a few pixels (usually less than five) showing about a factor of 5 or 10 larger count rate than the rest ($8-10\sigma$ above the average). In a detector plane image, we set five¹² highest pixel counts to the next-highest value.

Fig. 10b shows an example of the background subtracted detector plane images using single pixel trigger events in the combined set from the Cyg X-1 observation. The background subtraction eliminates most of the outstanding non-uniformities. For the Cyg X-1 observation, we generate such a background subtracted detector image every 12 s from 20:57:38 to 21:53:02 UT before the system reset (the power-cycle test) and from 22:31:08 UT to 22:39:32 after the reset. We produce the corresponding reconstructed sky images using a balanced correlation [ref] with the mask pattern using FFT. The detector image of 64×64 pixels is rebinned into 8192×8192 pixels in order to properly scale the mismatch of the mask (4.7 mm) and detector pixel pitch (5.1/2 mm)¹³. Each sky image (every 12 s) is then rebinned to 768×768 pixels covering down to the 10% coding fraction, aspected corrected and then

summed to produce the final image, weighted by the coding fraction.

5.2. Aspect Correction

Fig. 12a shows the aspect and pointing history of the Cyg X-1 observation. The star camera images are solved using astrometry.net [14] after post-processing the raw images to remove several streaks due to a defect in the CCD (see also [4]). The star camera images with a good aspect solution were only available for a small fraction of the observation (5 images before the reset around 21:15 UT and 63 images after the reset). For the pre-reset data, most of which do not have a matching star camera image, we correct the X-ray images using the azimuth and elevation given by the DGPS calibrated magnetometer and the digital readout of the elevation axis with shaft angle encoder (SAE) resolution of sub arcmin. For about 10 min of the usable post-reset data, we use the aspect information by the star camera images for the relative correction of the X-ray images.

Fig. 12b shows the relative offset between the aspect of the star camera and the aspect information calculated by the magnetometer and elevation axis. During the post-reset observation, the relative offset is within $20' - 30'$ in elevation and $\leq 10'$ in azimuth, but there seems to be a long term drift in the azimuth between the pre and post reset data, which can be as large as $50'$. This long term drift is the residual offset after the DGPS calibration, and it originates from the azimuth hysteresis of the mag-

¹²The final results are not sensitive to the exact choice of this number (from 5 to ~ 10) as long as the extreme outliers ($8-10\sigma$ above the average) are removed.

¹³The pixel pitch in a CZT crystal is 2.46 mm, but the gaps between the detectors make the overall pixel pitch equivalent to 2.55 mm (the detector pitch is 20.4 mm).

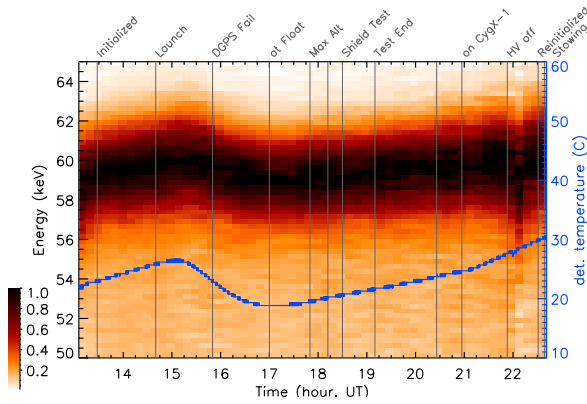


Fig. 11. Monitoring the gain variation during the flight using AmCal sources. The normalized energy histogram map as a function of time overlaid with the temperature of the FCB. The gain change ΔE (keV) $\approx 0.116\Delta T$ ($^{\circ}$ C).

netometer, which can be as large as a degree or two. In order to compensate for this offset, the aspect of the X-ray image around 21:15 is corrected to match the post-reset data, and the rest of the pre-reset data is corrected accordingly.

A caveat of the aspect correction described above is that the offset between the X-ray axis and the optical axis (or the axis of the star camera) must be known. A delay in the payload integration left no time for the X-ray vs. star camera boresight measurement before the launch. In order to resolve an ambiguity in aspect correction due to the unknown boresight, we first correct the pre-reset data according to the aspect information reported by the magnetometer and the elevation axis only relative to the image at 21:15, assuming there is no X-ray boresight offset. The combined image shows a point source of about 6.5σ at about 6° off the center of the X-ray image in the 30–100 keV band. Assuming this is Cyg X-1, one can estimate the X-ray boresight, which was calculated to be $31'$. This X-ray boresight value is reasonable, given the uncertainties in mounting the X-ray telescope and the star camera.

Assuming the $31'$ X-ray boresight offset, we reapply the aspect correction on the proper X-ray axis, and recombine the X-ray images. In the recombined image of the pre-reset data, the same point source now appeared at 6.8σ , indicating the proper boresighting has increased the signal. Finally we added the 10 min of the post-reset data using the aspect information given by the star camera images. In the final image, the point source appears at 7.2σ . This solution gives Cyg X-1 at the expected location with a reasonable boresight of the X-ray telescope to the

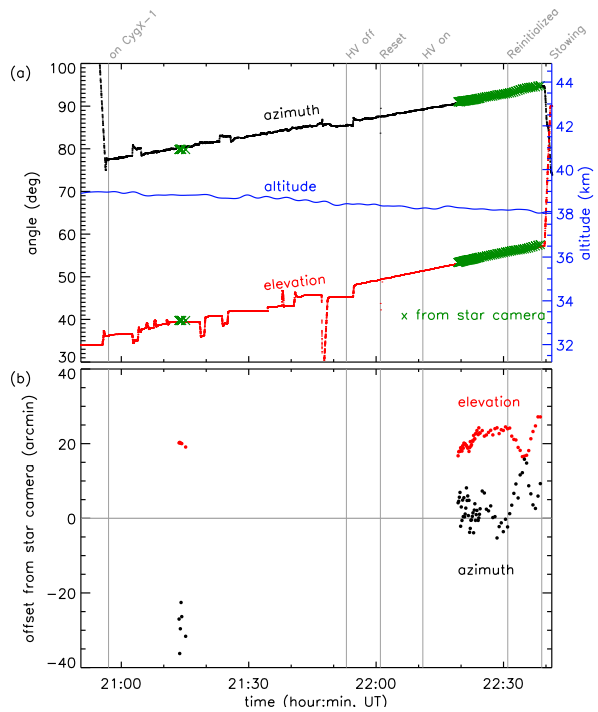


Fig. 12. (a) The aspect and pointing history and (b) the relative offset of the aspect given by the star camera vs. aspect given by the magnetometer and the elevation axis shaft angle encoder during the observation of Cyg X-1. The detector system was reset at around 22:00 UT for a test of in-flight recycling of power and initialization. For imaging and spectral analysis of Cyg X-1, the data taken from 20:57 to 21:53 UT (pre-reset: marked "on Cyg X-1" to "HV off") and from 22:31 to 22:39 UT (post reset: marked "Reinitialized" to "Stowing") were used.

star camera. Fig. 13a shows the reconstructed sky image in the 30–100 keV band. The X-ray and optical axis are marked by '+' and 'x'. The offset of Cyg X-1 from the X-ray axis is 6.4° , resulting in a partial coding fraction of 81% and thus 19% vignetting.

5.3. X-ray Spectrum of Cyg X-1

In order to calculate the X-ray spectrum of Cyg X-1, we repeat the above imaging procedure in the 30–50, 50–80, 80–125, and 125–190 keV bands. The thumbnail images in Fig. 13b show the reconstructed sky images around Cyg X-1 in these energy bands.

Due to the relatively large uncertainties ($\sim 30'$) of the aspect information given by the magnetometer and the elevation axis, a point source would appear somewhat broadened in the reconstructed sky images. For simplicity, we assume the source in the image is a point source and so the maximum of the

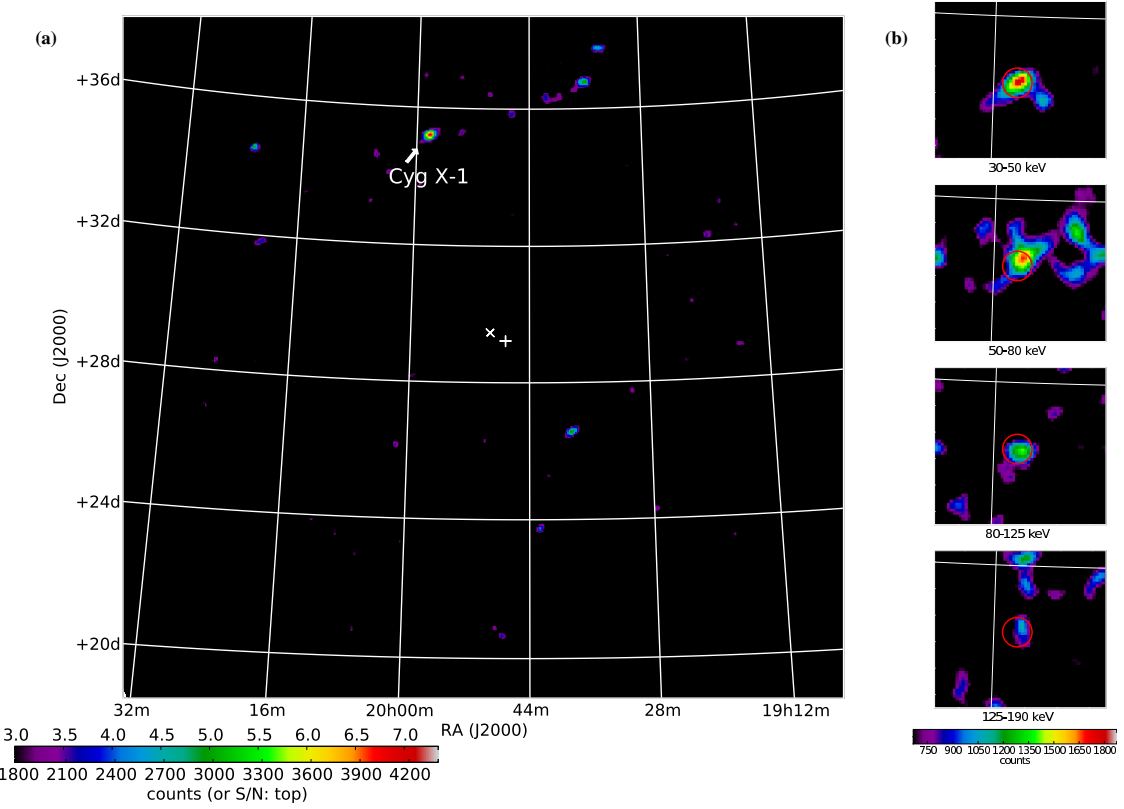


Fig. 13. Imaging Cyg X-1: (a) the reconstructed sky image in the 30–100 keV band above 60% coding fraction. (b) the $2^\circ \times 2^\circ$ thumbnail images around Cyg X-1 in the 30–50, 50–80, 80–125 and 125–190 keV bands. In (a), ‘+’ indicates the center of the X-ray image, and ‘x’ indicates the star camera axis. A $\sim 4\sigma$ blob around (R.A., DEC.) = (19h 40m, 26°) is a ghost image of Cyg X-1, caused by the cyclic nature of the mask pattern (URA). The noise around (19h 36m, 37°) is likely due to incomplete aspect correction, in particular, large elevation jitters, since they are aligned along the elevation direction from Cyg X-1. The red circles in (b) show the angular resolution (20' diameter).

“blob” in the source image gives the detected source counts. Using the maximum source counts is valid in our imaging procedure when the background counts are much greater than the source counts. In reality, this will give us a lower bound for the source counts.

We calculate the source counts in each band, and apply a series of corrections to get the incident rate, which include the average dead time (45%), the mask open fraction (38.7%), the average coding fraction (81%), the average coded mask auto-collimation effect (2.6%), the energy-dependent QE and atmospheric absorption. We assumed the QE of 86% in the 60–100 keV range and for the rest of the energies, we use a linear interpolation assuming 54% at 30 keV (where only photo peaks are collected with a ~ 30 keV threshold) and 68% at 200 keV (based on the total photon cross-section of CZT). For atmospheric absorption, we use the atmospheric depth of 3.5 g cm^{-2} at the average altitude 38.5 km [15] with the average elevation of

42.7° . In order to allow energy dependence, we use the attenuation of photons in the atmosphere in [16] (p 203). For both QE and atmospheric absorption, we calculate the energy bin averaged estimates using a power law spectrum of photon index $\Gamma=1.7$.

The resulting spectrum is shown in Fig. 14. The error bars along the x and y -axis represent the energy bin size and the statistical errors respectively. The red point shows the range of the source flux in 15–50 keV measured by *Swift*/BAT¹⁴ within 12 hours of the *ProtoEXIST1* observation. The closest BAT observations are about 1–2 hours before or after the *ProtoEXIST1* observation. The dashed line shows a representative hard X-ray spectral model of Cyg X-1 in the literature [17]. The observed flux is a bit lower than the other measurements but it is certainly in an acceptable range, given the high

¹⁴<http://heasarc.gsfc.nasa.gov/docs/swift/results/transients/>

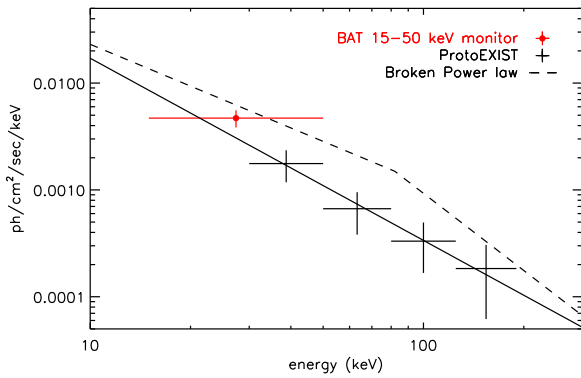


Fig. 14. The observed hard X-ray spectrum of Cyg X-1. The (red) data point represents the range of the observed flux in the 15–50 keV band by the BAT within 12 hours of the *ProtoEXIST1* observation. The broken power model (dashed) is from Steinle, et al, 1982 [17]. The solid line is a power law fit ($\sim E^{-\Gamma}$) to the data points, where the photon index $\Gamma = 1.7 \pm 0.5$.

X-ray variability of the source. The observed spectrum agrees with the known spectral models within 3σ and it can be fit by a simple power law model with photon index $\Gamma = 1.7 \pm 0.5$ (the solid line). The reduced χ^2 of the fit is small (~ 0.02) due to the large uncertainties. The observed spectrum is relatively harder, but the source detection in the hard X-ray band above 125 keV is marginal (Fig. 13b).

6. Summary and Future Development

We have successfully carried out the first high altitude (40 km) balloon flight of the wide-field hard X-ray telescope, *ProtoEXIST1*, employing the first generation of an advanced CZT imager. The CZT imager in *ProtoEXIST1* is, to our knowledge, the largest pixellated close-tiled CZT array at the moment (256 cm² with 2.5 mm pixels). The X-ray telescope performed excellently throughout the 7.5 hr flight. Despite a few problems in the new aspect and pointing system, we were able to detect Cyg X-1 at 7.2σ from about an hour observation, ~ 50 min of which was with relatively poor aspect and so with smearing in the elevation axis direction.

Encouraged by this success, we have begun the next phase of the program, *ProtoEXIST2*, which will have $4\times$ finer detector spatial resolution (pixel pitch: 0.6 mm) and also both lower energy threshold ($\sim 5 - 8$ keV) and better energy resolution (~ 2 keV). To accomplish this, a new ASIC, the Nu-

ASIC, developed for *NuSTAR*¹⁵ will be used in the 8×8 DCU close-tiled CZT detectors of *ProtoEXIST2*. The Nu-ASIC is developed in the same ASIC family line as the RadNET ASIC, so they share a similar basic operational architecture, which simplifies the transition. We will combine the Nu-ASIC front-end readout electronics with a new packaging and modularization architecture derived from the *ProtoEXIST1* system. For more details of the *ProtoEXIST2* detector development, see also [18].

7. Acknowledgement

This work was supported by NASA grants NNG06WC12G and NNX09AD76G to Harvard University, and NASA grant NNX10AJ56G to Washington University in St. Louis. We thank M. Burke (SAO engineering), N. Gehrels (GSFC), K. Dietz, C. M. Benson, B. Ramsey (MSFC), D. Huie (Univ. of Alabama Huntsville), W. R. Cook and F. Harrison (Caltech) for their support in the development and assembly of the *ProtoEXIST1* detector, telescope and gondola. We also thank the McDonnell Center for the Space Sciences for their support in the active CsI shield assembly, and the NASA CSBF balloon launching team for their excellent support.

References

- [1] Gehrels, N., et al, 2004, ApJ, 611, 1005.
- [2] Grindlay, J., et al, 2010, Proc. SPIE, 7732-59
- [3] Grindlay, J., et al, 2011, in preparation.
- [4] Allen, B., et al., 2010, Proc. SPIE 7732, 77324D
- [5] Allen, B., et al., 2011, in preparation.
- [6] Hong, J., et al, 2009, NIM Physics Res. Sec. A 605, 364
- [7] Cook, W. R., Burnham, J. A. & Harrison, F. A., 1998, Proc. SPIE, 3445, 347.
- [8] Harrison, F., et al, 2010, Proc. SPIE, 7732-27
- [9] Hong, J., et al, 2006, Proc. SPIE, 6219, 63190S
- [10] Luke, P. N., 1994, Applied Physics Letter, 65, 2885
- [11] Roques, J.P., 1987, Appl. Opt., 26, 3862
- [12] Busboom, A., Elders-Boll, H., & Schotten, H. D., 1998, Experimental Astronomy 8, 97
- [13] Gehrels, N., 1985, NIM Physics Res. Sec. A 239, 324
- [14] Lang, D., et al, 2010, AJ, 139, 1782
- [15] Stenov, T., 2004, High Energy Cosmic Rays, 2nd edition, Springer
- [16] Zombeck, M. V., et al, 1990, Handbook of Space Astronomy & Astrophysics, 2nd edition, Cambridge University Press
- [17] Steinle, H., et al, 1982, Astron. Astrophys., 107, 350
- [18] Hong, J., et al, 2010, Proc. SPIE 7732, 77321Y-1

¹⁵<http://www.nustar.caltech.edu/>